Aerospace Science and Technology 118 (2021) 107006

Contents lists available at ScienceDirect

Aerospace Science and Technology

www.elsevier.com/locate/aescte

Buckling-driven mechanisms for twisting control in adaptive composite wings

Jiayao Zhang, Chiara Bisagni *

Delft University of Technology, Faculty of Aerospace Engineering, Delft, Netherlands

ARTICLE INFO

Article history:
Received 29 May 2021
Received in revised form 20 July 2021
Accepted 1 August 2021
Available online 9 August 2021
Communicated by Jang-Kyo Kim

Keywords:
Buckling
Twisting
Morphing
Composite structures
Wing box
Multi-stable configurations

ABSTRACT

This study aims to design novel tailorable and effective mechanisms by controlling buckling behaviour in structural elements of a composite wing for future morphing application. Instead of the traditional design against buckling, the idea is to embrace this built-in instability by using the nonlinear post-buckling response to control stiffness changes which redistribute the load in the wing structure. To enable desired multi-stable configurations, three buckling-driven mechanisms are investigated by restraining the out-of-plane buckling deformation using point, area and maximum displacement constraints. Numerical studies of the proposed mechanisms are at first conducted on a composite plate and are later integrated to control twisting of a simplified thin-walled composite wing box. The proposed mechanisms offer effective design opportunities of multi-stable configurations and demonstrate the potential to realise morphing of composite wings employing controlled buckling behaviours in structural components.

1. Introduction

Buckling has long been considered a structural phenomenon characterised by a large deformation and therefore by losing the ability to sustain the designed loads. Several recent experimental studies, for example those reported in [1–3], show the possibility to allow composite stiffened panels of primary aeronautical components to work in the post-buckling field so to potentially reduce the structural weight. Besides, the development of analytical and numerical methods with current optimization algorithms [4–6] demonstrates a promising future of exceptionally reliable prediction on buckling performance.

This paper would like to take a further step and exploit the possibility of a paradigm shift on the design of aeronautical structures away from *design against buckling* and towards *novel performance through controlled buckling* to provide the structure of morphing capabilities. To design the embedded element for buckling, various methods can be implemented to trigger the intended configurations. Some studies in this direction can already be found in literature. For example, employing the residual stress field in cross-ply unsymmetrical laminates, Mattioni et al. [7] note the possibility to introduce multi-stability and to tune the shapes of the equilibrium states for morphing application. Further development of the piecewise combination of unsymmetrical laminates [8] reveals that, by designing the spatial distribution of more sections, it is possible to preserve the multi-stability while two loaded ends are clamped in a structure system. Other concepts propose to use the thermal behaviour of composite structures during curing period, which requires careful manufacturing and operational control. A few studies utilize the thermal residual stresses for obtaining bistable structures, considering the thermal behaviour using hybrid materials [9] or adopting curved tool plates in moulding [10,11].

In analogy to triggering buckling or bistability by introducing residual thermal stresses, the 3D assembly of laminates can prestress selective elements by clamps or welds in the interconnected structure, thus a residual stress field is embedded to achieve various buckling configurations of the system. The influence of those interconnected spots is investigated analytically by the study of different elastic boundary constraint on flutter and thermal buckling on composite panel [12] with Rayleigh-Ritz method, while the experimental tries went far beyond that. Vos et al. [13] present a new class of actuators with post-buckled prestressed piezoelectric elements which outperform the conventional piezoelectric actuators by increasing the deflection level up to three times. Applications are then expanded over ailerons, flaps and missile fins ranging from subsonic through supersonic [14]. Daynes and Weaver [15] propose an adaptive twisting mechanism by connecting laminates with a pre-bend and/or pre-twist manner. Due to the exis-

* Corresponding author at: Delft University of Technology, Faculty of Aerospace Engineering, Kluyverweg 1, 2629HS Delft, Netherlands.
E-mail address: c.bisagni@tudelft.nl (C. Bisagni).

https://doi.org/10.1016/j.ast.2021.107006

tence of geometric nonlinearity, the structure is capable of slowly moving between two equilibrium states with diverse angles of twist.

Solutions have been investigated to utilize elastic structural instability to modify the stiffness of certain structural elements and thus to trigger a load redistribution to realise not only shape changes [16] but changes of response to the aerodynamic loads due to aeroelasticity [17,18]. The change of torsional behaviour has been spotlighted in morphing aircraft designs by compliant mechanisms. The concept is designed to be purely passive, where the occurrence of selective shear buckling can be deliberately excited by specific aerodynamic loads [19]. In most of the cases presented in literature, the structure can only perform in two predefined configurations.

In a completely different sector, the sector of the micro-electrical mechanical systems, the wide implementation of mechanical-controlled buckling elements has been witnessed thanks to the noticeable improvement of precise fabrication techniques. Inspired by the ancient wisdom of origami, Yan et al. [20] came up with a buckling-oriented design scheme in which a spatial thickness variation is manufactured in the initial filamentary ribbon to trigger the targeted buckled configuration under compression. Seeing the elastic nature of buckling deformation, certain reversible configurations over intermediate states in the 2D to 3D transformation can be achievable with the assistance of further load or displacement control to support more real-time adjusting applications. Fu et al. [21] developed a mechanically guided buckling scheme where the different sequences of releasing the stretched substrate can trigger the stabilisation of two distinct buckling modes. The two ribbons are restraining one another at the connecting spot, which act to the same effect as a physical constraint to limit the transverse deflection and eventually directs it to deform in the second buckling mode. Zhao et al. [22] manages the introduction of torsional load into the ribbons to twist the 3D structure into the targeted chiral shape. Since the rotational force is well controllable by the cut pattern in the substrate, the post-buckling behaviour of the ribbons is well tailorable and predictable. Jiao et al. [23] studied the post-buckling behaviour with deflection constrained between an upper and lower bound by adding bilateral confinements along with the axially loaded micro composite films. The implemented sidewalls are further developed into irregular, i.e. discontinuously flexible and movable wall constraints. The tunability of the buckling mode obtained is guaranteed by the movable constraints.

In aeronautics, the wing design always focuses on the design [24,25], analysis and optimization [26,27] of the wing box, that is the main load-bearing structure. The advantage of mechanical-induced buckling design for morphing applications lies in a broad and intuitive design space to generate highly predictable multi-stable responses satisfying the requirements of controllability and robustness.

This paper presents the first steps of a buckling-driven methodology under development for composite wing boxes where the post-buckling behaviour of one or more spar webs can be controlled by out-of-plane deflection constraints, so that the wing twisting performances are tailored by the relative stiffness of the spar webs compared to the rest of the structure. In contrast with the aforementioned purely passive load-triggered control, the methodology imposes an active control that, at the sacrifice of limited amount of load and actuation energy, allows to gain the real-time controllability of the post-buckling behaviour and to enhance the adaptivity of the morphing wing structure to meet multi-stable tailorable situations.

In particular, this paper focuses on the design of the buckling-driven constraint mechanisms considering different structures of increasing complexity. The paper is structured as follows: Section 2 proposes three different mechanisms and the working principles described from a theoretical aspect. Section 3 provides the numerical studies of the proposed mechanisms on a composite plate. The viability of the twisting control is verified through numerical simulations applying the proposed mechanisms to a simplified wing box in Section 4 and to a simplified wing structure in Section 5. The conclusions of the study are reported in Section 6.

2. Design of buckling-driven mechanisms

The concept of either hindering or activating buckling deformation with the assistance of out-of-plane constraints is explored by realising three mechanisms and making reasonable extrapolation based on simplified models. The mechanisms are illustrated considering a plate loaded in compression in Fig. 1.

The first buckling-driven mechanism, here called *point constraint*, is represented in Fig. 1a, and is the physical restraint example discussed in classical textbooks. A point constraint is simply supported at x_A on the surface of the plate confining transverse deflection but leaving the in-plane displacements and rotations free. The y-coordinate of the point is taken on the symmetric line, where the maximum buckling deformation occurs. With the possible buckling modes limited to those satisfying the restraint, the plate deforms into the mode which requires the lowest strain energy.

A mechanism based on an extension of the previous concept is here called *area constraint* and is represented in Fig. 1b. In this mechanism, the same restriction as point constraint, i.e. simple support, is employed to constrain the only transverse deformation extended to an area. The area is determined by two separation lines parallel to the loaded edges, $x = x_1$ and $x = x_2$. The plate then consists of the constrained area S and two free-to-buckle parts.

The third mechanism consists in constraining the buckling deformation with one or two rigid surfaces parallel to the plate, as represented in Fig. 1c. Once the buckled plate gets in contact with the confinements, the out-of-plane deformation of the local area in the contact zone is blocked. The adjacent local areas continue to buckle thus extends the contact zone with the confinement surfaces. The capability to stop the buckling deformation is mostly defined by the distance z between the undeformed mid-plane and the confining bounds. This distance defines the maximum buckling displacement the plate can reach. Therefore, the mechanism is called *maximum displacement constraint*.

The three buckling-driven mechanisms are all based on the idea of creating more equilibrium paths for the composite structures, introducing additional boundary conditions. They are described in more details and applied in the following Sections.

3. Plate buckling analyses

All three mechanisms are first studied on a composite plate loaded in compression. The plate is made of unidirectional plies with carbon fibres and epoxy resin IM7/8552, which properties are reported in Table 1. The plate has length a of 900 mm, width b of 300 mm, and is made of 8 plies for a total thickness t of 1 mm. The lay-up here considered is symmetric quasi-isotropic $[0/45/-45/90]_S$, but both the plate aspect ratio and the lay-up can be promising design variables to be optimised in future works. Also variable-stiffness design can be investigated to enlarge the possible design space [28–31].

The plate is simple supported on all four edges. Other boundary conditions such as free and clamped unloaded edges are considered as well. To design the plate to be a buckling-oriented element in a structural system, a relatively low buckling load with a larger post-buckling regime is desired. Free boundaries cannot provide

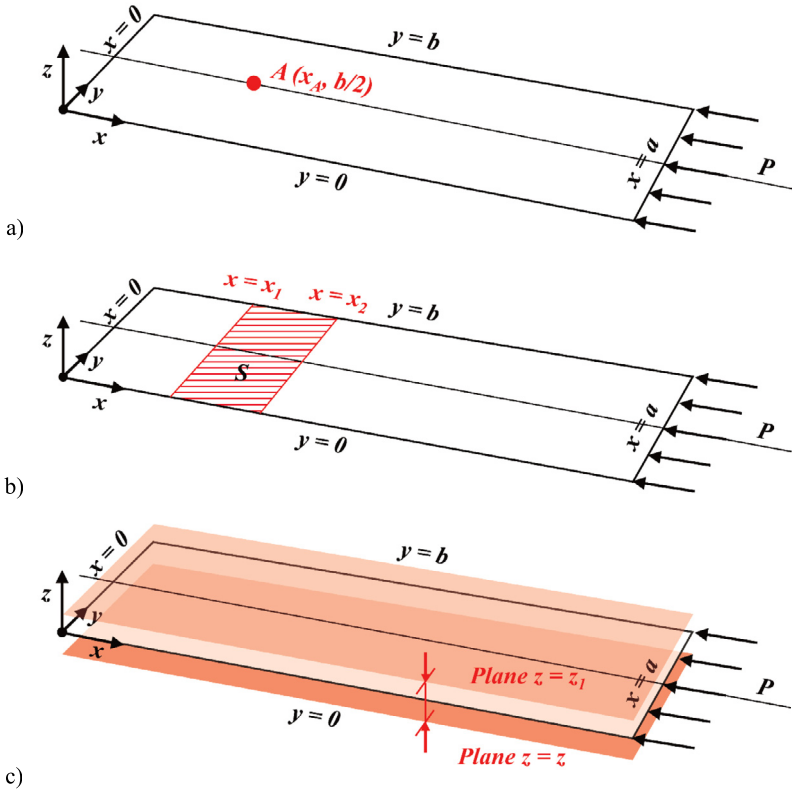

Fig. 1. Buckling-driven mechanisms: a) point constraint, b) area constraint, c) maximum displacement constraint.

Table 1
Ply properties of unidirectional IM7/8552 composite.

E_{11} [MPa]	E_{22} [MPa]	G_{12} [MPa]	ν	ρ [kg m^{-3}]	t_{ply} [mm]
150000	9080	5290	0.32	1570	0.125

a stable post-buckling configuration, and clamped edges push the critical buckling load too high. Thus, the simply-supported boundary is selected here to have the boundary stiffness of the original plate comparable to the stiffness variation introduced by the constraints.

Finite element analyses are conducted using ABAQUS [32] to investigate the linear and nonlinear buckling behaviour and the possible design space. The composite plates are modelled using a single layer of quadrilateral conventional shell elements S4R with a mesh length of 10 mm. Modelling the thin-walled structures here analysed using shell elements increases computational efficiency compared to solid elements while still successfully capturing the in-plane response and out-of-plane bending response as the thickness is small compared to the other dimensions.

Critical buckling load and displacement are obtained by eigenvalue analyses. For studying the post-buckling behaviour, a quasi-static procedure is performed with dynamic implicit solver for a time period 1 s with maximum 10000 increments and the maximum increment size set as 0.015 s. The damping factor alpha is 0.1 and no numerical extrapolation is applied. Implicit dynamic method is chosen as it is the most accurate within the time efficiency required for design iterations.

The first four modes of the $[0/45/-45/90]_S$ plate without any constraint mechanisms, obtained by eigenvalue analysis, present 2, 3, 4 and 1 half-waves, respectively, as shown in Fig. 2. Performing the dynamic implicit analysis, the post-buckling stiffness is determined, and it results reduced to about half compared to the pre-buckling stiffness.

The plate configuration without any constraint mechanisms is taken as baseline. The goal of implementing the proposed mechanisms is to modify the plate post-buckling stiffness.

To better visualize the three mechanisms, the side-viewed deformed shapes of the plates are plotted with a scaling factor for the out-of-plane displacement of 30 in Fig. 3.

At first, the point constraint mechanism is investigated. The results of four analyses considering different positions of the point constraints are reported in Table 2, and compared to the baseline. The corresponding load paths and post-buckling deformation contours are reported in Fig. 4 and Fig. 5, respectively. It is intuitive that, by choosing the point location at half-length position, the behaviour is exactly as the baseline, because the point constraint fits the first buckling shape. With the simply supported point at one-third length position, the plate is forced to deform into its second mode with three half-waves and the critical buckling load is increased by 12%. Indeed, in this case, the additional restraint stiffens the plate and the buckling modes allowed by the constraint require higher loads to trigger. Besides, the point constraint at one-third length position reduces the post-buckling stiffness to 88%, as additional buckles are activated and the deformed shape with more half-waves is more compliant. When the plate is constrained at other locations, such as one-fourth length or one-fifth length, it deforms into three uneven half-waves, instead of the third eigenmode of the baseline plate with four uniform half-waves.

Considering post-buckling stiffness, most of the point locations reduce the stiffness because they activate additional buckles and naturally the deformed shape with more half-waves is more compliant. However, if the point positions close to one edge as $x_A = a/5$, the post-buckling stiffness is then dominated by the larger section with 4/5 plate length. The section deforms in the same two half-waves but shorter in length than the half-waves in the baseline. Hence the post-buckling stiffness increases. In conclusion, the effect on post-buckling stiffness depends on point constraint location (i.e. x_A) and varies between 12% reduction to 3% increase.

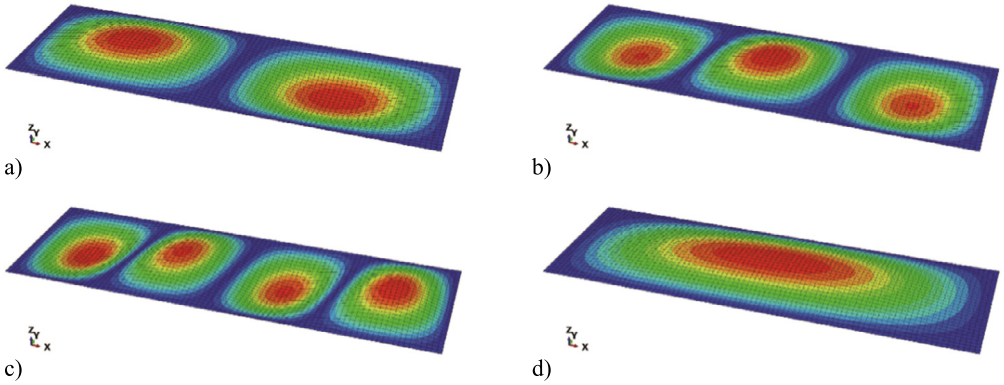

Fig. 2. First four buckling modes of $[0/45/-45/90]_S$ plate loaded in compression: a) mode 1, b) mode 2, c) mode 3, d) mode 4.

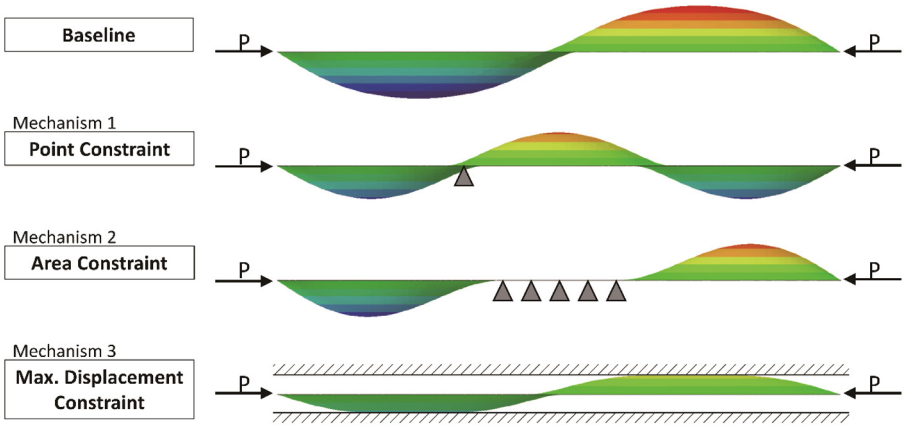

Fig. 3. Deformed shape of $[0/45/-45/90]_S$ plate loaded in compression with buckling-driven mechanisms.

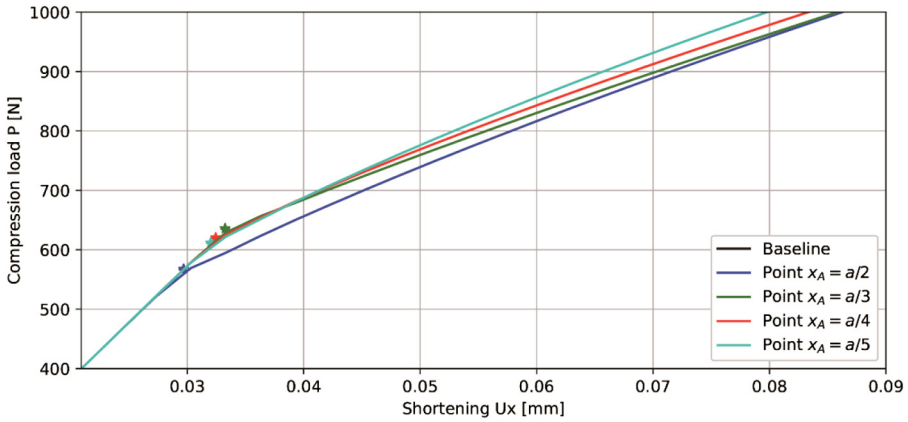

Fig. 4. Load-shortening curves of point constrained plate loaded under compression.

Table 2
Buckling and post-buckling results of point constrained plate.

	Baseline	Point $x_A = a/2$	Point $x_A = a/3$	Point $x_A = a/4$	Point $x_A = a/5$
P_{cr} [N]	568	568	636	620	612
U_{cr} [mm]	0.0297	0.0297	0.0333	0.0324	0.0320
K_{pre} [kN/mm]	19.12	19.12	19.12	19.12	19.12
K_{post} [kN/mm]	8.35	8.35	7.33	7.92	8.61

The most effective constraint location results to be where the buckling mode can be altered to exactly the next buckling mode. The optimal effect on the reduction of the post-buckling stiffness, by adding a single point constraint, is thus determined by the stiffness difference between two adjacent buckling shapes.

The area constraint mechanism is expected to impose stronger effects on the plate buckling performance. For simplification, an identical one-fifth length area is adopted for all analyses and is moved along the plate to study the effect of different locations. The difference with point constraint is the higher order of restriction imposed on buckling displacement, as within the constraining area both deflection and curvature are zero. To maintain continuity from the free-to-buckle parts to the constrained area, the curvature gradually reduces approaching zero at the edge of the constrained area. The curvature of the plate cannot be passed through this area, so the plate practically consists of two separate free-to-buckle parts. The results of two representative analyses are reported in Table 3 and Fig. 6–7. The most effective constraint location is in the middle of the plate where the onset of buckling is signifi-

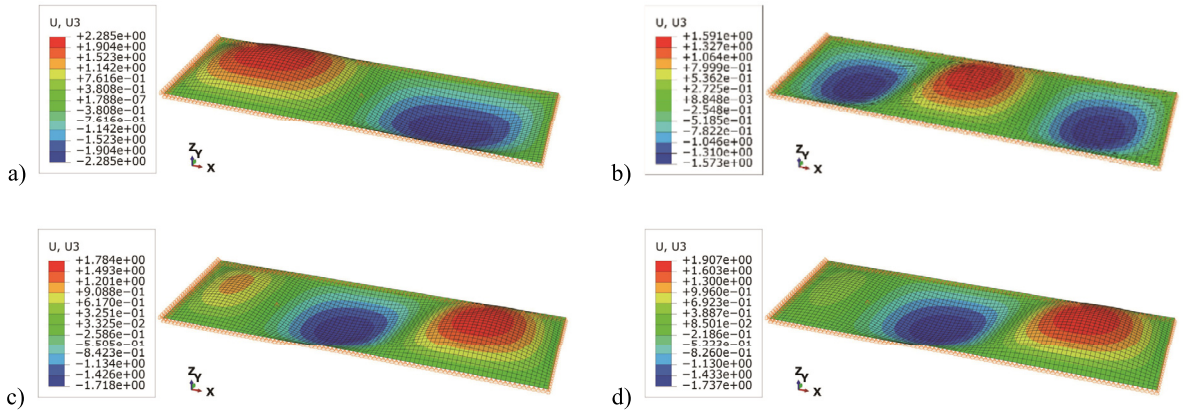

Fig. 5. Out-of-plane deformation of point constrained plate loaded under 1000 N compression: a) Point $x_A = a/2$, b) Point $x_A = a/3$, c) Point $x_A = a/4$, d) Point $x_A = a/4$. (For interpretation of the colours in the figure(s), the reader is referred to the web version of this article.)

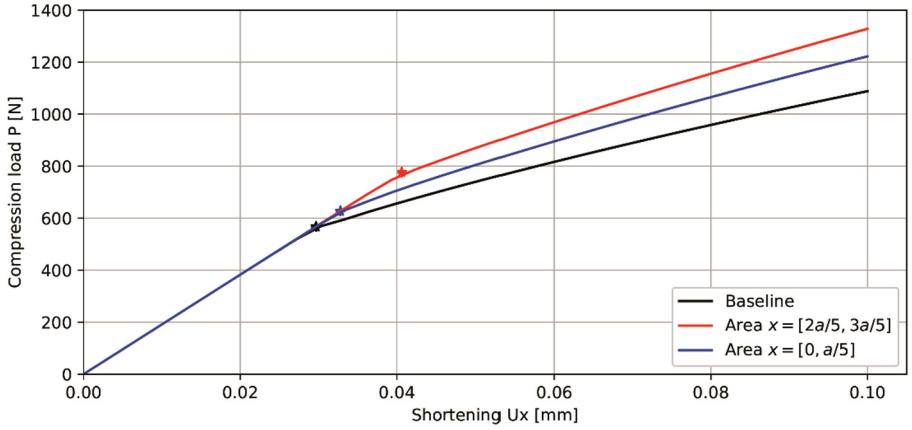

Fig. 6. Load-shortening curves of area constrained plate loaded under compression.

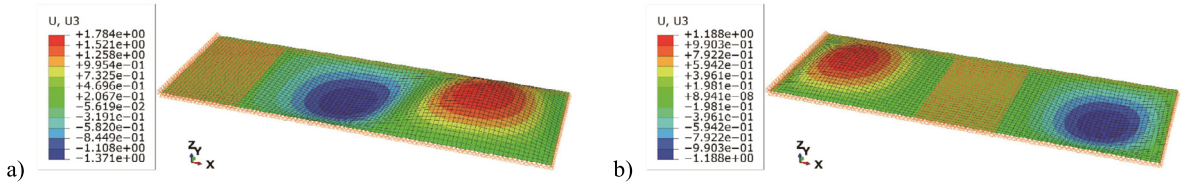

Fig. 7. Out-of-plane deformation of area constrained plate loaded under 1000 N compression: a) Area $[x_1, x_2 = 0, a/5]$, b) Area $[x_1, x_2 = 2a/5, 3a/5]$.

Table 3
Buckling and post-buckling results of area constrained plate.

	Baseline	Area $[x_1, x_2 = 0, a/5]$	Area $[x_1, x_2 = 2a/5, 3a/5]$
P_{cr} [N]	568	627	777
U_{cr} [mm]	0.0297	0.0328	0.0406
K_{pre} [kN/mm]	19.12	19.12	19.12
K_{post} [kN/mm]	8.35	9.64	9.91

cantly delayed by 37% and the post-buckling stiffness is enhanced by 19%. The enhancement of stiffness is realised by reducing the effective length for buckling deformation of the full plate length. The general effect on post-buckling stiffness is determined by the combination of location and length of the constrained area.

In the maximum displacement constraint mechanism, upper and lower bounds are established for the out-of-plane displacement by adding two rigid confinement surfaces and implementing contact between those surfaces and the plate. As the deformation of the confinements is not of interest, they are modelled as analytical rigid surfaces. Frictionless contact with sufficiently small time increments is implemented to capture the contact effect. It is observed that, for the baseline plate without any constraint applied, the out-of-plane displacement reaches over 2 mm. Thus, the chosen mechanisms are double-side constrained with 2 mm distance each side, single-side with 2 mm distance, and double-side with 1 mm. The maximum displacement constraint has no influence before the buckled plate gets contact with the confinements, so it has no effect on the buckling load and on the early phase of post-buckling stiffness. When the compression load increases, the plate buckles until the top or bottom deformation makes physical contact with any of the confining surfaces. At this point the out-of-plane deflection is blocked while the neighbouring area continues to deform. From the moment the contact validates, the post-buckling stiffness increases by a large amount, as shown in Table 4.

Unlike the first two active mechanisms that control the post-buckling shape and the stiffness change by moving the point and area constraints, the maximum displacement constraint is semi-active, meaning that once the confinements are placed, the post-buckling stiffness change can be automatically triggered when the

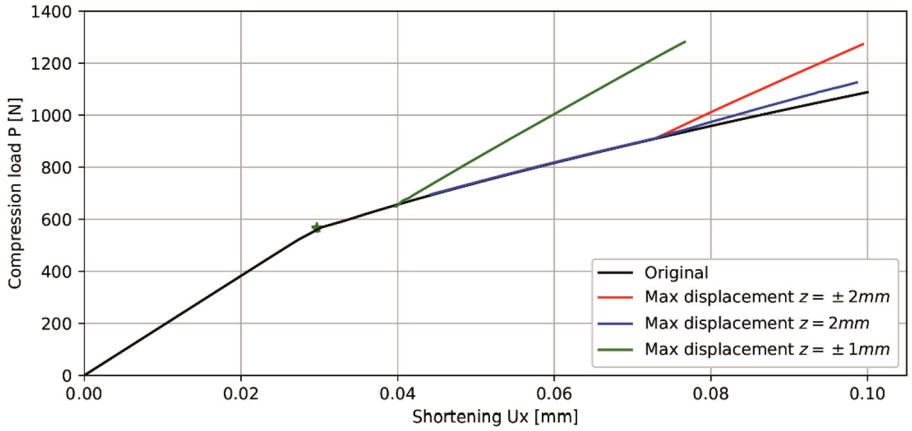

Fig. 8. Load-shortening curves of maximum displacement constrained plate loaded under compression.

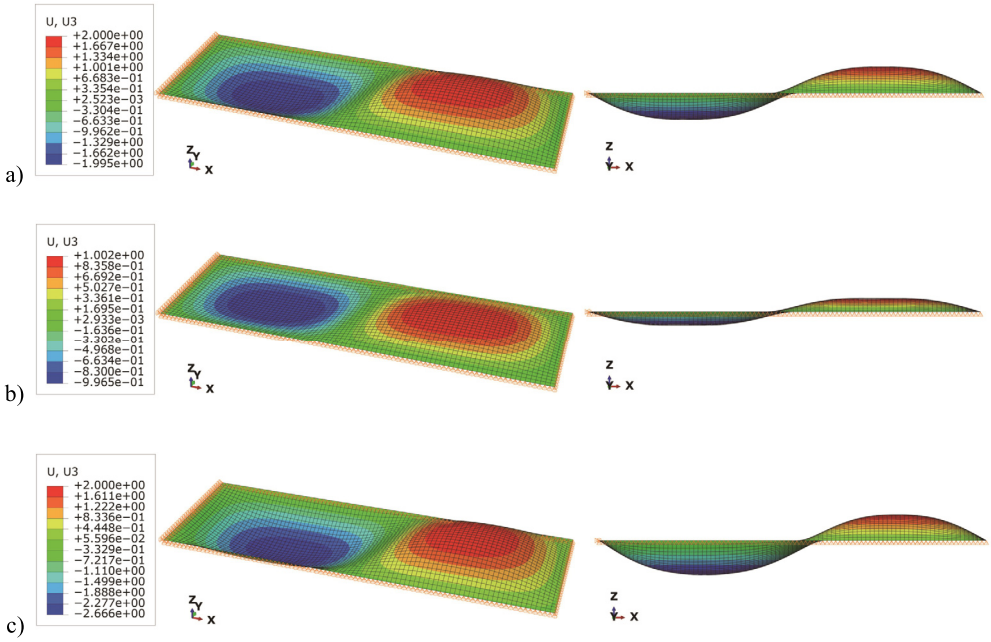

Fig. 9. Out-of-plane deformation of maximum displacement constrained plate loaded under 1100 N compression: a) Max displacement $z = \pm 2$ mm, b) Max displacement $z = \pm 1$ mm, c) Max displacement $z = 2$ mm.

Table 4
Buckling and post-buckling results of maximum displacement constrained plate.

	Baseline	Max displacement $z = \pm 2$ mm	Max displacement $z = \pm 1$ mm	Max displacement $z = 2$ mm
P_{cr} [N]	568	568	568	568
U_{cr} [mm]	0.0297	0.0297	0.0297	0.0297
K_{pre} [kN/mm]	19.12	19.12	19.12	19.12
K_{post} [kN/mm]	8.35	13.71	16.89	8.29

out-of-plane displacement reaches the set bounds. This can be observed in the load paths in Fig. 8.

The effect of this buckling-stopper maximum displacement constraint is significant on post-buckling stiffness, with a variation up to 102% for the case of double-side with 1 mm where the contact mechanism is triggered with a lower compression level and the contact zones with maximum deformation grow larger. By removing the confinement on one side, the deformed shape demonstrates asymmetry in the two half-waves. The out-of-plane deformations are reported in Fig. 9.

If the onset of buckling is considered, the most effective mechanism is the one-fifth plate length area constraint followed by point constraint. More importantly the effect on post-buckling stiffness varies for the different mechanisms from plus 102% to minus 8%. The effect of the point constraint relies entirely on the variation of post-buckling stiffness between different buckling shapes. The other two mechanisms block the buckling deformation in a certain region so that only elastic shortening is allowed. For maximum displacement constraint, this region is the contact zone which varies for every load increment, while for area constraint it is the pre-set restricted area which remains constant. The area constraint modifies the buckling mode as well.

The best size and position of the constraints could have been investigated considering an optimization problem, where the design variables are searched in a domain defined by several conditions to minimize an objective function. However, while the design variables are clear as they consist in the position and size of the constraints, as well as the geometrical and material limits, it is hard to define the objective function. From structure design aspects what is searched is the tailorability with an acceptable level

of mass and energy consumption, and not exactly the maximum shape change or stiffness change.

4. Buckling-driven mechanisms in a simplified wing box

A simplified model of a single-bay wing box between two ribs is analysed to verify whether these mechanisms can be implemented into wing primary structural elements. In particular, the rear spar of the wing box is designed to be the buckling-driven component.

Some simplifications are applied to the wing box structure. Firstly, the cross-section of the wing box is assumed to be a uniform rectangular profile with height H of 300 mm and width W of 500 mm. It has no sweep in the direction of wingspan hence the distance between two ribs is the length L taken equal to 900 mm. Therefore, the front and rear spars, the upper and lower skins are rectangular panels. Secondly, because the aim is to investigate the effect of the implemented buckling-driven elements on the whole structure, the stiffness of the rear spar is deliberately designed to be relatively low such that buckling can appear firstly and almost only in it. The rear spar has 8 layers of IM7/8552 with a quasi-isotropic $[0/45/-45/90]_S$ lay-up, while the other three panels of the box have 24 layers made of identical material with $[0/45/-45/90]_{3S}$ lay-up. Finally, beam-type multi-point constraints are introduced by enforcing the distance between the central reference point and the nodes at the tip and root to keep the rectangular shape of these sections. The boundary conditions and the load are applied to the reference points of the multi-point constraints and distributed to the ribs accordingly. Fixed boundary conditions are imposed at the root rib and concentrated force at the tip rib.

Three typical load conditions are analysed independently: compression P, shear S and torsion T. The structure is illustrated in Fig. 10, with the three buckling-driven mechanisms: point constraint (Fig. 10a), area constraint (Fig. 10b) and maximum displacement constraint (Fig. 10c).

The wing box under compression P shows a small stiffness reduction ability of buckling, about 5%, and the stiffness modification abilities of post-buckling mechanisms range from −5% to 6%, both of which are not so relevant. The wing box under shear S gives similar results as torsion T. As the wing box under torsion demonstrates the promising ability of considerable buckling-induced stiffness changes, offering a broad and accessible design range, and as the main load in aircraft wing is torsion, the main results under torsion are here presented.

The critical buckling torque T_{cr} obtained from the eigenvalue analysis results equal to 0.885 kNm, and the critical tip rotation Θ_{cr} equal to 0.291×10^{-3} rad. In the dynamic implicit analysis, the rear spar of the wing box buckles with a mode shape consisting of two symmetric half-waves, one buckles outward and one inward, with a skewed angle of about 45 degree. The buckling out-of-plane deformation at the torque equal to 2 kNm, which is about 2.3 times the critical buckling torque T_{cr}, is reported in Fig. 11 with an out-of-plane displacement scaling factor of 30.

When loaded by torque up to 2.3 times the critical buckling torque, without any mechanism applied, the buckling of the rear spar results in 22% torsional stiffness reduction of the entire wing box. Besides, relocation of shear centre is inspected. This relocation is about 12% of the wing box width (from 28% to 16%) towards the front spar.

Some of the results obtained using the buckling-driven mechanisms applied to the simplified wing box are reported in Table 5. By smartly choosing the location, the point constraint mechanism alters the buckling deformation to the next buckling mode, and enhances the post-buckling stiffness of the baseline configuration by 2%. With the area constraint, the post-buckling stiffness enhancement varies from 10% to 97% offering a broad and accessible design range. The effect of maximum displacement constraint is only on the post-buckling response and becomes effective when the buckling deformation of the rear spar is large enough to get into contact with the constraints. The contact stops the further out-of-plane displacement and thus increases the post-buckling stiffness from 10% to 20%. The capability of this mechanism is between the area constraint and the point constraint, as it allows a certain level of buckling but within defined confinement.

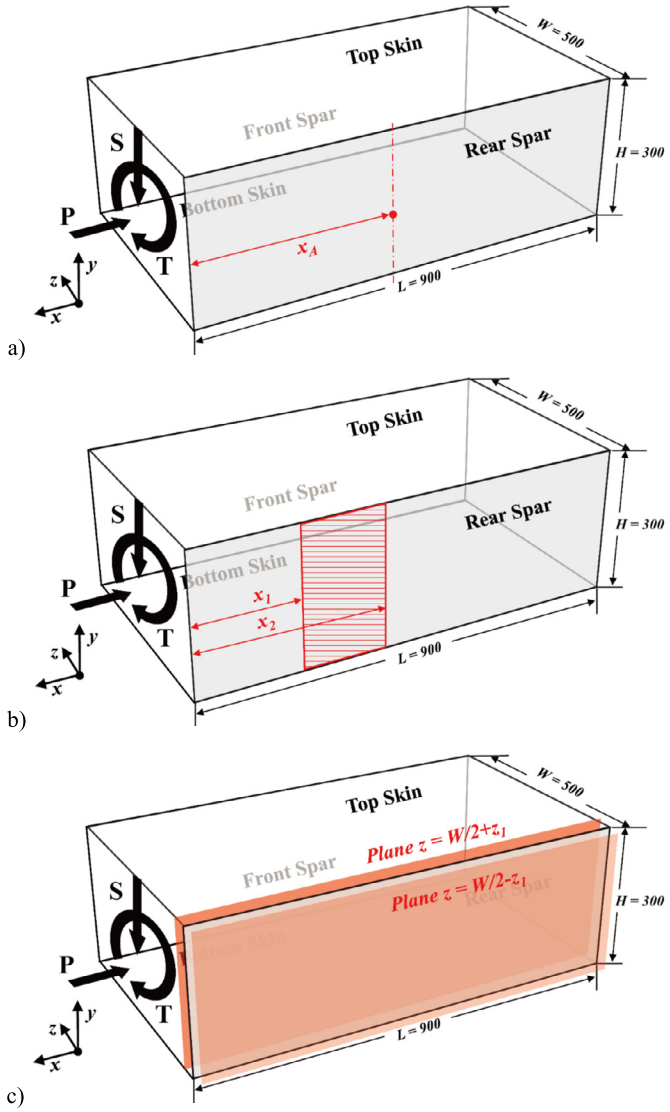

Fig. 10. Buckling-driven mechanisms on the rear spar of the simplified wing box: a) point constraint, b) area constraint, c) maximum displacement constraint.

Since all nonlinear post-buckling deformations are considered as quasi-static processes, the variation of mechanisms can create rapid jumps among the torque-rotation curves, providing the potentiality of multi-stable configurations combining different load paths.

One possible load path is taken as example to show possible applications controlling the implementation and removal of the proposed mechanisms and varying the locations of the constraints. The path is presented in Fig. 12 with a bold curve and makes the most of the stiffness modification capability playing on maximum displacement constraint and area constraint. This path develops a

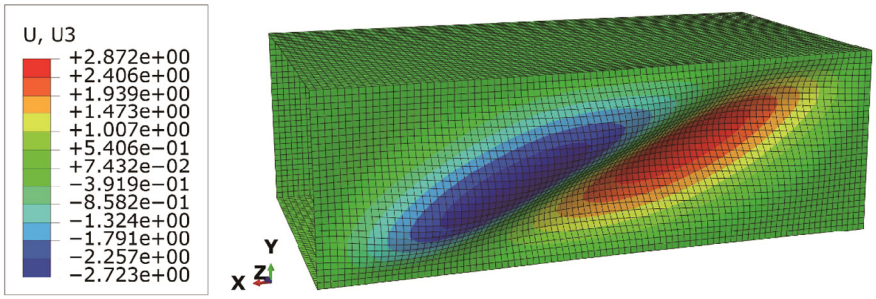

Fig. 11. Post-buckling out-of-plane deformation of the simplified wing box.

Table 5
Buckling and post-buckling results of wing box under torsion.

	Baseline	Point $x_A = L/3$	Area $[0.2L, 0.4L]$	Area $[0.4L, 0.6L]$	Max displacement $z = \pm 1.5$ mm	Max displacement $z = \pm 2$ mm
T_{cr} [kN m]	0.885	0.909	1.811	2.029	0.885	0.885
Θ_{cr} [10^{-3} rad]	0.291	0.298	0.360	0.518	0.291	0.291
K_{pre} [10^6 N m rad^{-1}]	3.039	3.042	5.017	3.909	3.039	3.039
K_{post} [10^6 N m rad^{-1}]	2.385	2.439	4.697	3.650	2.824	2.601

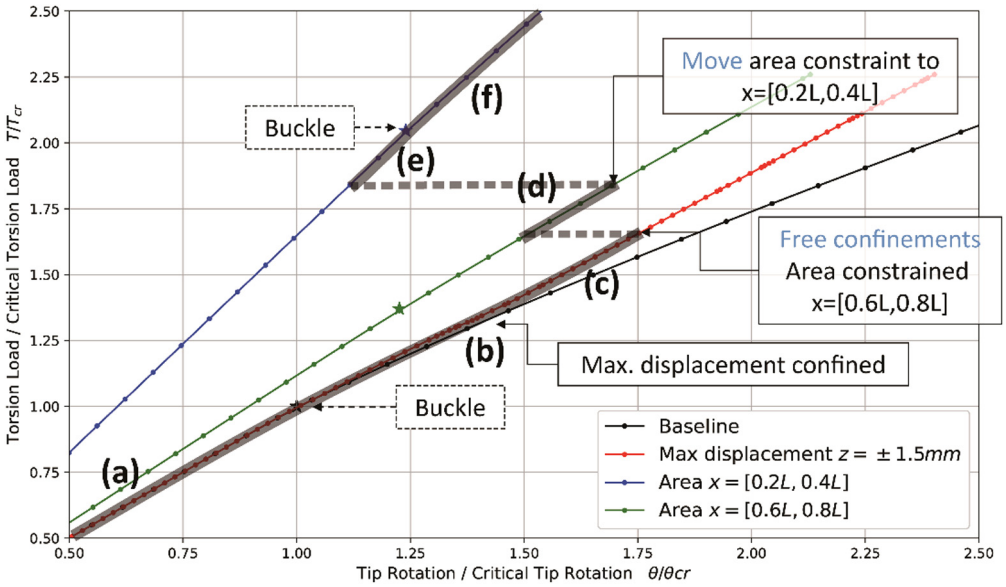

Fig. 12. Controlled wing box torque-rotation load path.

rising torsional stiffness, from 0.78 K_0 to 1.65 K_0, where K_0 is defined as the torsional stiffness of the baseline wing box without mechanisms. This significant change in torsional stiffness can be observed by the change of the slope within the bold curve. The out-of-plane deformation contours of the representative stable configurations are shown in Fig. 13 with out-of-plane displacement scaling factor of 30 and the same contour scale from −0.5 mm to 1.5 mm.

The post-buckling stiffness is sensitive to the applied constraints with up to 97% change compared to the wing box without constraints. In addition to the effect on stiffness change, the buckled rear spar relocates the shear centre of the wing box. These two effects provide the possibility to control wing twisting by controlling the buckling behaviour of one single element embedded. Besides, the design of parameters in each buckling-driven mechanism and the sequence to implement them enriches the space of possible stable conditions.

5. Buckling-driven mechanisms to control wing twisting

The possibility to modify the buckling load and the post-buckling stiffness, creating multi-stable states using the different buckling-driven mechanisms is here explored on a simplified wing structure. The proposed mechanisms have the potential to modify wing twisting by controlling the buckling behaviour of one single element embedded.

A simplified wing structure is analysed. The structure consists of five identical boxes like the single wing box just presented, laid out end-to-end to form a box beam with longer span and same cross-section. The wing model represents a full-length simplified wing with five rib-bays as illustrated in Fig. 14, where the airfoils are sketched to distinguish the front and rear spars, but not included in the model. The wing model presents the same assumptions previously adopted. First, the wing geometry is perfectly straight with no sweep or no instalment angle between any

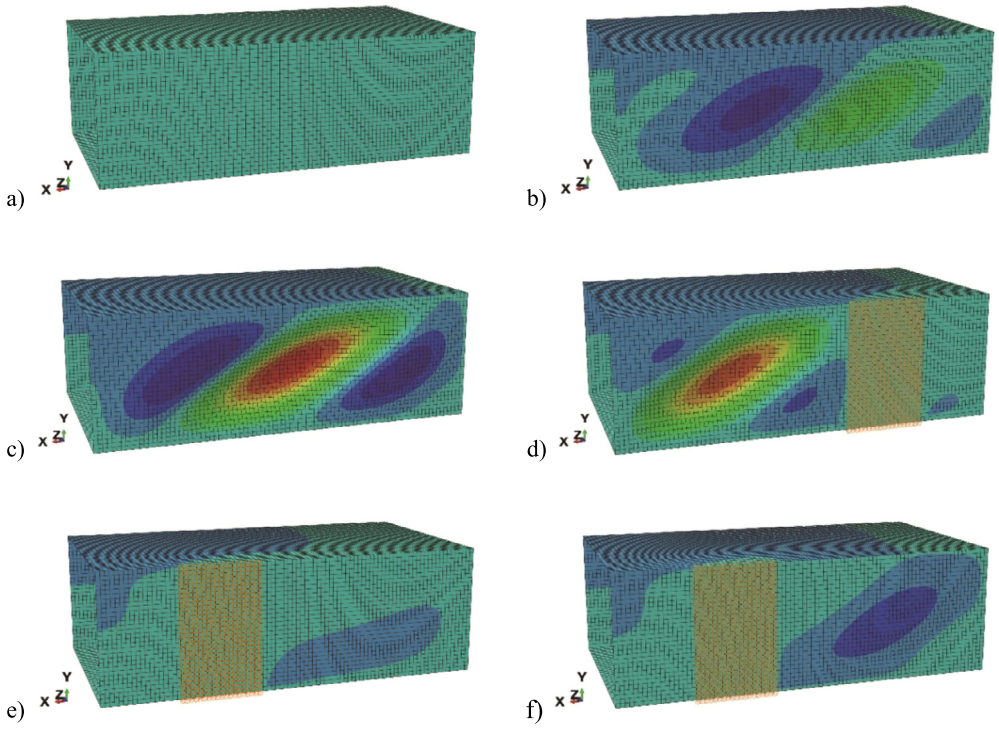

Fig. 13. Wing box deformation during the torque-rotation load path: a) Undeformed wing box, $K_a = K_0$; b) Buckled wing box without constraints, $K_b = 0.78K_0$; c) Maximum displacement constraint at $z = \pm 1.5$ mm, $K_c = 0.93K_0$; d) Area constraint at $[0.6L, 0.8L]$, $K_d = 1.02K_0$; e) Unbuckled wing box with area constraint at $[0.2L, 0.4L]$, $K_e = 1.65K_0$; f) Buckled wing box with area constraint at $[0.2L, 0.4L]$, $K_f = 1.55K_0$.

two of the ribs. The length of the wing L results five times the single box length, so equal to 4500 mm, and the cross-sectional properties remain constant with width W equal to 500 mm and height H equal to 300 mm. Second, the rear spar is designed to be the slender element while front spar, top and bottom skin panels to be stiffer. The symmetric quasi-isotropic layups used in the single wing box are implemented, with 8 plies for the rear spar and 24 plies for the other panels. Moreover, each of the six ribs is modelled as the same multi-point constraints to preserve the rectangular section. The displacements and the rotations in all six rib frames follow the corresponding reference points, respectively. The boundary conditions and the load are applied to the reference points and distributed to the ribs accordingly. The wing root is assumed to be clamped.

The wing model is analysed without and with mechanisms to investigate the post-buckling performances when a torque moment is applied.

At first, the baseline wing without any mechanism is analysed. An eigenvalue analysis and a dynamic implicit analysis are performed, and the results are reported in Table 6. Since the rotation angle accumulates along the span direction, the wing tip rotation of 1.45×10^{-3} rad is five times the one of the single wing box. Besides, it is possible to note that the post-buckling stiffness reduction, respect to the pre-buckling stiffness, is equal to about 22%, and this value is similar to the one obtained for the single wing box.

In the proposed wing structure, it is possible to trigger the buckling deformation of the rear spar in each rib bay independently, leading to additional design aspects of the buckling-driven proposed mechanisms, the location and the number of the constrained rib bays. Although there are several practical limitations that need to be investigated, in this study it is assumed that the entire rear spar can be implemented with mechanical systems to apply the desired constraints and to explore the potential of controlling buckling behaviour in the different rib bays.

The results obtained considering just the area constraint mechanisms are here presented, and in particular the results of the analyses constraining the first rib bay (the closest to the root), constraining the third one and constraining all rib bays are reported in Table 6. The enhancement on torsion stiffness is noticeable as both K_{pre} and K_{post} boost to 600% respect to the baseline configuration. In this configuration no one single rib bay is free to buckle with the original aspect ratio. It is equivalent to add stiffeners to the rear spar to prevent the whole wing from buckling.

The adoption of the area constraint in the first rib bay is least effective in changing the structure response, but it could be also the least energy-consuming for the mechanical system to enforcing the constraint. This suggests that, if sufficient stiffness change is obtained, the constraints should remain as close to the wing root as possible. With more rib bays constrained, the enforcing energy is distributed to every constrained area.

A representation of the buckled wing with five bays and area constraint mechanism implemented on the rear spar of the first bay is shown in Fig. 15.

Ideally the stiffness required for wing structures during the entire flights is not constant but depends on the flight condition. With a fixed structure, the stiffness is optimized for a specific flight condition. Introducing buckling-driven mechanisms, the structure can adapt different stiffness for different load conditions with the possibility to obtain an adaptive composite wing. Moreover, shape change impacts the stress distribution of the structure and may change the failure mode thus may play a beneficial role in structural design.

6. Conclusions

The next generation aircraft will require lighter and more flexible structures, with the same or increased level of safety. This study has presented a proof-of-concept of a new idea where the boundary conditions are modified to govern when buckling occurs

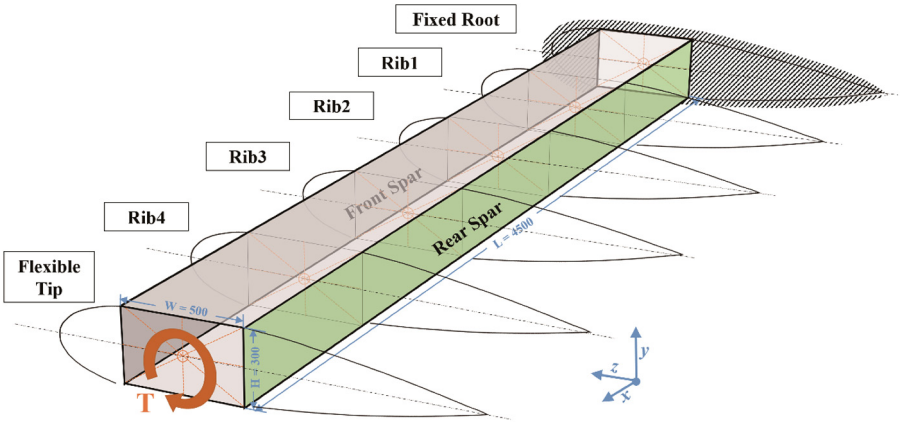

Fig. 14. Sketch of the analysed wing structure.

Table 6
Buckling and post-buckling results for wing under torsion with area-constrained mechanisms.

	Baseline	Area $[0.2L, 0.4L]$ in first rib bay	Area $[0.2L, 0.4L]$ in middle bay	Area $[0.2L, 0.4L]$ in all rib bays
T_{cr} [kN m]	0.885	0.885	0.885	2.237
Θ_{cr} [10^{-3} rad]	1.454	1.339	0.806	0.515
K_{pre} [kN m rad^{-1}]	607.2	659.8	1097.5	4310.9
K_{post} [kN m rad^{-1}]	469.7	527.0	935.5	3397.2

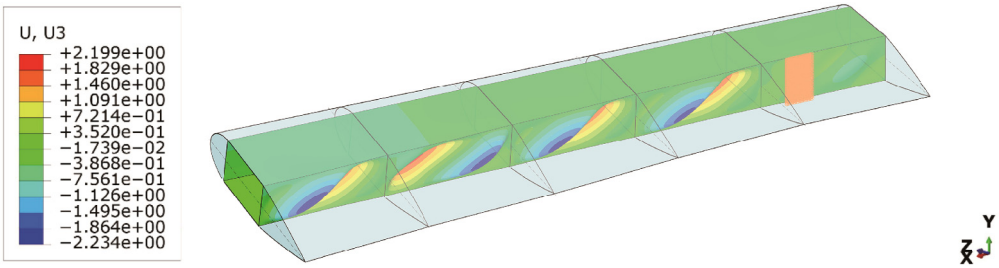

Fig. 15. Buckled wing with area constraint mechanisms implemented on the first rib bay and highlighted contour of the out-of-plane displacements.

and to tune multiple non-traditional post-buckling stable configurations. These structures will be able to adapt their shape during different flight conditions, acting on two of the biggest levers for the future of clean aviation: reduced weight and increased efficiency.

Aiming for the implementation in a composite wing to complete promising morphing tasks, three buckling-driven mechanisms are proposed to enable desired buckling configurations with specific stiffness by restraining the out-of-plane displacement with point, area and maximum displacement constraints. The constraints are simulated numerically, and the capability of realising the change of buckling load and post-buckling stiffness is discussed considering at first a composite plate. Then, the implementations of such buckling-driven mechanisms on the rear spar of a simplified wing box and later on a simplified wing structure under torsion are investigated. The promising ability of considerable buckling-induced stiffness changes to control twisting is demonstrated offering a broad and accessible design space. The post-buckling stiffness is sensitive to the constraints applied and up to 600% change comparing to the one of the wing box without constraints can be obtained. In addition to the effect on stiffness change, the buckled rear spar relocates the shear centre of the wing box. These two effects provide the potential to control wing twisting by controlling the buckling behaviour of one single embedded element.

The study has exploited a paradigm shift on the design guidelines away from design against buckling and towards novel performance through controlled buckling. It can provide a new design strategy for morphing capabilities but still requires an extensive research effort to carry out a practically feasible design. Prototypes will be manufactured as the feasibility of such designs needs to be validated experimentally.

Declaration of competing interest

The authors declare that they have no known competing financial interests or personal relationships that could have appeared to influence the work reported in this paper.

References

[1] C. Bisagni, C.G. Dávila, Experimental investigation of the postbuckling response and collapse of a single-stringer specimen, Compos. Struct. 108 (2014) 493–503.
[2] C.G. Dávila, C. Bisagni, Fatigue life and damage tolerance of postbuckled composite stiffened structures with initial delamination, Compos. Struct. 161 (2017) 73–84.
[3] P. Cordisco, C. Bisagni, Cyclic buckling tests under combined compression and shear on composite stiffened panels, AIAA J. 47 (12) (2009) 2879–2893.
[4] V. Gulizzi, V. Oliveri, A. Milazzo, Buckling and post-buckling analysis of cracked stiffened panels via an X-Ritz method, Aerosp. Sci. Technol. 86 (2019) 268–282.
[5] K. Tian, L. Huang, Y. Sun, K. Du, P. Hao, B. Wang, Fast buckling load numerical prediction method for imperfect shells under axial compression based on pod and vibration correlation technique, Compos. Struct. 252 (2020) 112721.

[6] H. Wagner, H. Köke, S. Dähne, S. Niemann, C. Hühne, R. Khakimova, Decision tree-based machine learning to optimize the laminate stacking of "composite cylinders for maximum buckling load and minimum imperfection sensitivity, Compos. Struct. 220 (2019) 45–63.
[7] F. Mattioni, A. Gatto, P.M. Weaver, M.I. Friswell, K. Potter, The application of residual stress tailoring of snap-through composites for variable sweep wings, in: 47th AIAA/ASME/ASCE/AHS/ASC Structures, Structural Dynamics, and Materials Conference, 2006, Paper no. AIAA 2006-1972.
[8] I.K. Kuder, A.F. Arrieta, P. Ermanni, Design space of embeddable variable stiffness bi-stable elements for morphing applications, Compos. Struct. 122 (2015) 445–455.
[9] H. Li, F. Dai, P. Weaver, S. Du, Bistable hybrid symmetric laminates, Compos. Struct. 116 (2014) 782–792.
[10] J. Ryu, J.P. Kong, S.W. Kim, J.S. Koh, K.J. Cho, M. Cho, Curvature tailoring of unsymmetric laminates with an initial curvature, J. Compos. Mater. 47 (25) (2013) 3163–3174.
[11] H. Lee, J.G. Lee, J. Ryu, M. Cho, Twisted shape bi-stable structure of asymmetrically laminated cfrp composites, Composites, Part B, Eng. 108 (2017) 345–353.
[12] Y. Chai, F. Li, Z. Song, C. Zhang, Influence of the boundary relaxation on the flutter and thermal buckling of composite laminated panels, Aerosp. Sci. Technol. 104 (2020) 106000.
[13] R. Vos, R. Barrett, R. de Breuker, P. Tiso, Post-buckled precompressed elements: a new class of control actuators for morphing wing UAVs, Smart Mater. Struct. 16 (3) (2007) 919–926.
[14] R. Vos, R. Barrett, Post-buckled precompressed techniques in adaptive aerostructures: an overview, J. Mech. Des. 132 (3) (2010) 031004.
[15] S. Daynes, P.M. Weaver, Stiffness tailoring using prestress in adaptive composite structures, Compos. Struct. 106 (2013) 282–287.
[16] F. Nicassio, G. Scarselli, F. Pinto, F. Ciampa, O. Iervolino, M. Meo, Low energy actuation technique of bistable composites for aircraft morphing, Aerosp. Sci. Technol. 75 (2018) 35–46.
[17] I.K. Kuder, A.F. Arrieta, W.E. Raither, P. Ermanni, Variable stiffness material and structural concepts for morphing applications, Prog. Aerosp. Sci. 63 (2013) 33–55.
[18] N. Tsushima, T. Yokozeki, W. Su, H. Arizono, Geometrically nonlinear static aeroelastic analysis of composite morphing wing with corrugated structures, Aerosp. Sci. Technol. 88 (2019) 244–257.
[19] F. Runkel, A. Reber, G. Molinari, A.F. Arrieta, P. Ermanni, Passive twisting of composite beam structures by elastic instabilities, Compos. Struct. 147 (2016) 274–285.
[20] Z. Yan, F. Zhang, J. Wang, F. Liu, X. Guo, K. Nan, Q. Lin, M. Gao, D. Xiao, Y. Shi, Y. Qiu, H. Luan, J.H. Kim, Y. Wang, H. Luo, M. Han, Y. Huang, Y. Zhang, J.A. Rogers, Controlled mechanical buckling for origami-inspired construction of 3D microstructures in advanced materials, Adv. Funct. Mater. 26 (16) (2016) 2629–2639.
[21] H. Fu, K. Nan, W. Bai, W. Huang, K. Bai, L. Lu, C. Zhou, Y. Liu, F. Liu, J. Wang, M. Han, Z. Yan, H. Luan, Y. Zhang, Y. Zhang, J. Zhao, X. Cheng, M. Li, J. Woo Lee, Y. Liu, D. Fang, X. Li, Y. Huang, Y. Zhang, J.A. Rogers, Morphable 3D mesostructures and microelectronic devices by multistable buckling mechanics, Nat. Mater. 17 (3) (2018) 268–276.
[22] H. Zhao, K. Li, M. Han, F. Zhu, A. V´azquez-Guardado, P. Guo, Z. Xie, Y. Park, L. Chen, X. Wang, H. Luan, Y. Yang, H. Wang, C. Liang, Y. Xue, R.D. Schaller, D. Chanda, Y. Huang, Y. Zhang, J.A. Rogers, Buckling and twisting of advanced materials into morphable 3D mesostructures, Proc. Natl. Acad. Sci. 116 (27) (2019) 13239–13248.
[23] P. Jiao, A.H. Alavi, W. Borchani, N. Lajnef, Micro-composite films constrained by irregularly bilateral walls: a size-dependent post-buckling analysis, Compos. Struct. 195 (2018) 219–231.
[24] A. Roy, R. Mukherjee, Three dimensional rectangular wing morphed to prevent stall and operate at design local two dimensional lift coefficient, Aerosp. Sci. Technol. 107 (2020) 106312.
[25] M. Esposito, M. Gherlone, P. Marzocca, External loads identification and shape sensing on an aluminum wing box: an integrated approach, Aerosp. Sci. Technol. (2021) 106743.
[26] M. Esposito, M. Gherlone, Composite wing box deformed-shape reconstruction based on measured strains: optimization and comparison of existing approaches, Aerosp. Sci. Technol. 99 (2020) 105758.
[27] J. Li, M. Zhang, Data-based approach for wing shape design optimization, Aerosp. Sci. Technol. 112 (2021) 106639.
[28] S.F. Pitton, S. Ricci, C. Bisagni, Buckling optimization of variable stiffness cylindrical shells through artificial intelligence techniques, Compos. Struct. 230 (2019) 111513.
[29] E. Labans, C. Bisagni, Buckling and free vibration study of variable and constant-stiffness cylindrical shells, Compos. Struct. 210 (2019) 446–457.
[30] P. Hao, X. Yuan, C. Liu, B. Wang, H. Liu, G. Li, F. Niu, An integrated framework of exact modeling, isogeometric analysis and optimization for variable-stiffness composite panels, Comput. Methods Appl. Mech. Eng. 339 (2018) 205–238.
[31] P. Hao, D. Liu, K. Zhang, Y. Yuan, B. Wang, G. Li, X. Zhang, Intelligent layout design of curvilinearly stiffened panels via deep learning-based method, Mater. Des. 197 (2021) 109180.
[32] Dassault Systemes, Abaqus Analysis Guide, 2019.